Monthly Notices
of the
ROYAL ASTRONOMICAL SOCIETY

MNRAS **460,** 966–979 (2016)
Advance Access publication 2016 April 22

doi:10.1093/mnras/stw938

Secular models and Kozai resonance for planets in coorbital non-coplanar motion

C. A. Giuppone[1,2]★ and A. M. Leiva[1]

[1] *Universidad Nacional de Córdoba, Observatorio Astronómico, Laprida 854, X5000BGR Córdoba, Argentina*
[2] *Universidad Nacional de Córdoba, Observatorio Astronómico, IATE, Laprida 854, X5000BGR Córdoba, Argentina*

Accepted 2016 April 19. Received 2016 April 19; in original form 2015 December 14

ABSTRACT

In this work, we construct and test an analytical model and a semi-analytical secular model for two planets locked in a coorbital non-coplanar motion, comparing the results with the restricted three-body problem. The analytical average model replicates the numerical *N*-body integrations, even for moderate eccentricities ($\lesssim$0.3) and inclinations ($\lesssim 10^\circ$), except for the regions corresponding to quasi-satellite and Lidov–Kozai configurations. Furthermore, this model is also useful in the restricted three-body problem, assuming a very low mass ratio between the planets. We also describe a four-degree-of-freedom semi-analytical model valid for any type of coorbital configuration in a wide range of eccentricities and inclinations. Using an *N*-body integrator, we have found that the phase space of the general three-body problem is different to the restricted case for an inclined system, and we establish the location of the Lidov–Kozai equilibrium configurations depending on the mass ratio. We study the stability of periodic orbits in the inclined systems, and find that apart from the robust configurations, L_4, AL_4 and QS, it is possible to HARBOUR two Earth-like planets in orbits previously identified as unstable (U) and also in Euler L_3 configurations, with bounded chaos.

Key words: planets and satellites: dynamical evolution and stability – methods: analytical – celestial mechanics – Planetary systems.

1 INTRODUCTION

The three-body problem has been studied for decades, particularly for the coorbital problem. The coorbital problem or 1:1 mean motion resonance (1:1 MMR) occurs with a central star and two planets. The periods of the planets are almost the same, although the resonance acts to avoid collisions between the bodies. During the last few years, several approaches have been developed to find new types of regular orbit for this resonance. In particular, surface of sections in parametric spaces (Hadjidemetriou, Psychoyos & Voyatzis 2009; Hadjidemetriou & Voyatzis 2011), semi-analytical models (Giuppone et al. 2010) and analytical models (Robutel & Pousse 2013) have been used.

Efforts have been made to determine the possibility of detecting coorbital planets through the radial velocity signal (Giuppone et al. 2012; Dobrovolskis 2013; Leleu, Robutel & Correia 2015), transit detection (Ford & Gaudi 2006) or transit timing variations if one or both planets transit the stellar disc (Ford & Holman 2007; Haghighipour, Capen & Hinse 2013; Vokrouhlický & Nesvorný 2014). Although we still do not know the details of the dominant formation and evolutionary processes of these planetary systems, as well as their type, a general discussion has been established about whether or not the planets can be captured in the MMR 1:1.

Particularly in the non-coplanar case, we think that it is important to compare the general problem to the restricted problem because these results can be applied to our own Solar system. For example, the dynamical structure of the coorbital region provides a possible origin for coorbital satellites of planets. As pointed out by Namouni (1999) and Mikkola et al. (2006), transitions from horseshoe (HS) or tadpole (TP) orbits to quasi-satellite (QS) orbits can be thought of as a transport mechanism of distant coorbiting objects to a state of temporary or permanent capture around the planet. Once trapped, additional mechanisms provide subsequent permanent capture, for example, collisions with other satellites, mass growth of the planet or the drag of the circumplanetary nebula. This model can be useful even in the formation of the Janus–Epimetheus system through collisions. Recently, Morais & Namouni (2016) showed that resonant capture in coorbital motion is present for both prograde and retrograde orbits.

Classical celestial mechanics books (Moulton 1914; Brouwer & Clemence 1961) deal with Lagrangian equilibrium points and the orbits around them in the context of the restricted three-body problem (RTBP), namely, HS and TP orbits. However, some other equilibrium orbits have been identified recently. As far as we know, three different kinds of periodic orbit can be found in the averaged general three-body problem. It is convenient to describe the configurations with two angles $(\sigma, \Delta\varpi) = (\lambda_2 - \lambda_1, \varpi_2 - \varpi_1)$, where λ_i are the mean longitudes and ϖ_i are the longitudes of the pericentre of the planets. Apart from the well-known

★ E-mail: cristian@oac.unc.edu.ar

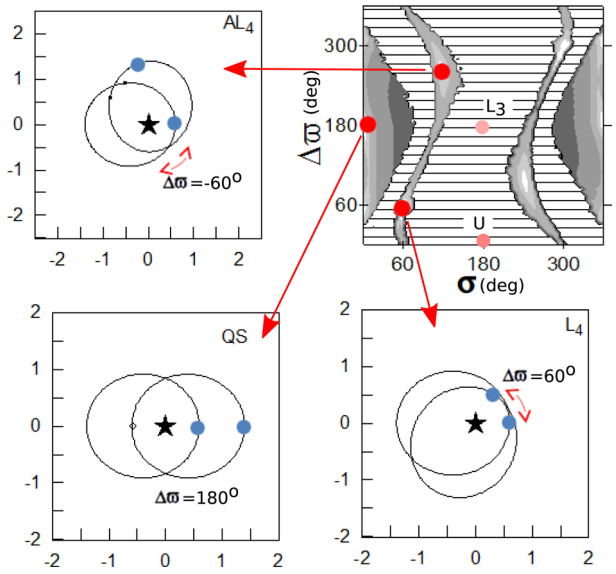

Figure 1. The top right-hand panel shows a dynamical map of the plane $(\sigma, \Delta\varpi)$ with the colour scale representing the oscillation amplitude of σ. Initial osculating elements correspond to two Jupiter planets orbiting a 1 $M_\odot$ star at 1 au with initial osculating eccentricities $e_i = 0.4$. The grey-scale indicates the amplitude of oscillation for σ and the dashed region corresponds to unstable configurations. In the remaining panels, we identify the three periodic orbits, QS, L_4 and AL_4, and plot their representation in the plane (x, y) with the star at the origin. Initial conditions for both planets are shown with blue circles, with m_1 located along the x-axis. Both axis directions are fixed.

equilateral configurations, located at the classical equilibrium Lagrangian points (L_4 and L_5) with angles $(\sigma, \Delta\varpi) = (\pm 60^\circ, \pm 60^\circ)$, QS orbits and anti-Lagrangian orbits (AL_4 and AL_5) are present. For low eccentricities, anti-Lagrangian orbits are located at $(\sigma, \Delta\varpi) = (\pm 60^\circ, \mp 120^\circ)$. One anti-Lagrangian solution AL_i is connected to the corresponding L_i solution through the σ-family of periodic orbits in the averaged system (the solutions with zero amplitudes of the σ oscillation). The QS orbits are characterized by oscillations around a fixed point, which is always located at $(\sigma, \Delta\varpi) = (0^\circ, 180^\circ)$, independently of the planetary mass ratio and eccentricities. In the top right-hand panel of Fig. 1, we construct a dynamical map with a grey-scale indicating the amplitude of oscillation of σ on the plane $(\sigma, \Delta\varpi)$ identifying the equilibrium orbits. Each of the other plots shows the orbital representation of some configurations in (x, y) astrocentric Cartesian coordinates. We focus our attention on the L_4 and AL_4 configurations, because the L_5 and AL_5 configurations are dynamically equivalent to the former [see Hadjidemetriou et al. (2009) and Giuppone et al. (2010)]. Additionally, in Fig. 1, we mark with light circles the location of the Euler configuration, L_3, and the centre of the unstable family (U) studied by Hadjidemetriou et al. (2009) and afterwards related with the L_3 configuration by Robutel & Pousse (2013). We pay special attention to both configurations in the final section. Note that L_3 is located at $(\sigma, \Delta\varpi) = (180^\circ, 180^\circ)$, while the unstable configuration U is located at $(\sigma, \Delta\varpi) = (180^\circ, 0^\circ)$.

In Section 2, we present the Hamiltonian analytical model with elliptic expansions and explore the validity of the average model. Also, we compare the results with direct N-body integrations. In Section 3 we introduce the average semi-analytical model for the three-body problem in the non-coplanar case, extending previous results, and compare to numerically filtered integrations. Following, in Section 4, we focus on the study of 3D equilibrium orbits, particularly on the Lidov–Kozai (LK) resonance with the different models. Finally, conclusions are presented in Section 5.

2 ANALYTICAL MODEL

Classical expansions of the disturbing function do not converge when the semi-major axis ratio is $\simeq 1$, and consequently they are not appropriate to model the coorbital resonance. Then, our intention is to give an easy-to-handle Hamiltonian to describe the motion within this resonance. We consider a system of two planets with masses m_i moving around a star with mass m_0 with inclinations lower than 90°. We do not include additional planets or dissipative forces. Each planetary orbit is described by six orbital elements: semi-major axis a, eccentricity e, inclination i, longitude of pericentre ϖ, mean longitude in orbit λ and longitude of the node Ω. Alternatively, we can use the arguments of the pericentre $\omega = \varpi - \Omega$, mean anomaly $M = \lambda - \varpi$ and true anomaly f.

We write the Hamiltonian following Laskar & Robutel (1995), using a canonical set of variables introduced by Poincaré with astrocentric positions of the planets $\mathbf{r}_i$ and barycentric momentum vectors $\mathbf{p}_i$. The pairs $(\mathbf{r}_i, \mathbf{p}_i)$ form a canonical set of variables with the Hamiltonian given by

$$H = H_0 + U + T. \tag{1}$$

Here, H_0 is the Keplerian part (sum of the independent Keplerian Hamiltonians), U is the direct part and T is the kinetic part of the Hamiltonian, written in terms of the canonical variables $(\mathbf{r}_i, \mathbf{p}_i)$ as

$$H_0 = -\sum_{i=1}^{N} \left(\frac{p_i^2}{2\beta_i} - \frac{m_0 m_i}{||\mathbf{r}_i||} \right),$$

$$U = -\mathcal{G} \sum_{i,j=1\ i\neq j}^{N} \frac{m_i m_j}{\Delta_{ij}},$$

$$T = \sum_{i,j=1\ i\neq j}^{N} \frac{\mathbf{p}_i \cdot \mathbf{p}_j}{m_0}, \tag{2}$$

where $\mathcal{G}$ is the gravitational constant, $\beta_i = m_0 m_i/(m_0 + m_i)$ and $\Delta_{ij} = ||\mathbf{r}_i - \mathbf{r}_j||$.

In the three-body problem, the barycentric momenta $\mathbf{p}_i$ are related to the heliocentric velocities $\dot{\mathbf{r}}_i$ by the following expressions:

$$\mathbf{p}_1 = \frac{m_1}{m_0 + m_1 + m_2} [(m_0 + m_2)\dot{\mathbf{r}}_1 - m_2 \dot{\mathbf{r}}_2]$$

$$\mathbf{p}_2 = \frac{m_2}{m_0 + m_1 + m_2} [(m_0 + m_1)\dot{\mathbf{r}}_2 - m_1 \dot{\mathbf{r}}_1]. \tag{3}$$

For the planetary case $m_i \ll m_0$, then

$$\mathbf{p}_1 \simeq m_1 \dot{\mathbf{r}}_1 + \frac{m_1 m_2}{m_0} (\dot{\mathbf{r}}_1 - \dot{\mathbf{r}}_2)$$

$$\mathbf{p}_2 \simeq m_2 \dot{\mathbf{r}}_2 + \frac{m_1 m_2}{m_0} (\dot{\mathbf{r}}_2 - \dot{\mathbf{r}}_1). \tag{4}$$

The distance Δ between the planets is

$$\Delta^2 = r_1^2 + r_2^2 - 2 r_1 r_2 \cos\phi \tag{5}$$

where ϕ is the angle between the vectors $\mathbf{r}_1$ and $\mathbf{r}_2$:

$$\cos\phi = \frac{\mathbf{r}_1 \cdot \mathbf{r}_2}{r_1 r_2}. \tag{6}$$

We then expand positions and velocities in eccentricities e_j and inclinations $s_j = \sin(i_j/2)$ obtaining an analytic expansion for the Hamiltonian $\mathcal{H}$. Also, we keep the coefficients up to the order

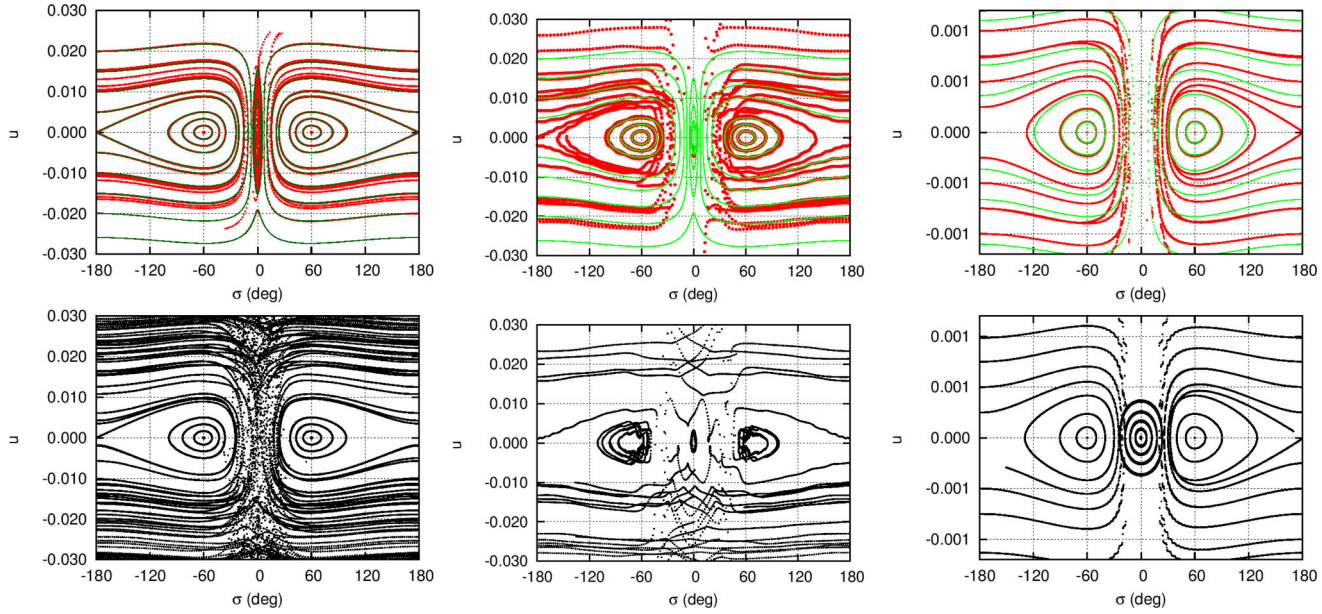

Figure 2. Top row: Phase space described by initial conditions integrated using $\mathcal{H}$ and $\mathcal{H}_{00}$ in the plane (u, σ). Shown are Jupiter-like planets in quasi-circular orbits (left-hand panel), Jupiter-like planets in eccentric orbits (middle panel) and Earth-like planets in eccentric orbits (right-hand panel). Bottom row: The same initial conditions integrated with the *N*-body code for 400 yr. See text for details.

$\mathcal{O}(e_j^2)$, $\mathcal{O}(s_j^2)$ and $\mathcal{O}(m_j)$. Then, we integrate over the fast angle $\lambda_1 + \lambda_2$, recovering the averaged analytical Hamiltonian $\mathcal{H}_2$ as

$$\begin{aligned}
\mathcal{H}_2 &= \mathcal{H}_{00} + \mathcal{G}m_1m_2\mathcal{H}_{22},\\
\mathcal{H}_{00} &= -\frac{\beta_1\mu_1}{2a_1} - \frac{\beta_2\mu_2}{2a_2} + \mathcal{G}m_1m_2\left(\frac{\cos\sigma}{\sqrt{a_1a_2}} - \frac{1}{\tilde{\Delta}}\right),\\
\mathcal{H}_{22} &= H_{2000}\,(e_1^2 + e_2^2) + H_{1100}\,e_1e_2\\
&\quad + H_{0020}\,(s_1^2 + s_2^2) + H_{0011}\,s_1s_2,
\end{aligned} \tag{7}$$

where

$$\begin{aligned}
\mu_i &= \mathcal{G}(m_0 + m_i),\\
\sigma &= \lambda_2 - \lambda_1,\\
\tilde{\Delta} &= \sqrt{a_1^2 + a_2^2 - 2a_1a_2\cos(\sigma)}.
\end{aligned} \tag{8}$$

$\mathcal{H}_{00}$ has zero-order terms in eccentricities and inclinations, and $\mathcal{H}_{22}$ has order two terms, formally:

$$\begin{aligned}
H_{2000} &= -\frac{\cos(\sigma)}{2\sqrt{a_1a_2}}\\
&\quad + \frac{a_1a_2}{8\tilde{\Delta}^5}\left[4\cos(\sigma)(a_1^2 + a_2^2) + a_1a_2(5\cos(2\sigma) - 13)\right],\\
H_{1100} &= \frac{\cos(\Delta\varpi - 2\sigma)}{\sqrt{a_1a_2}} + \frac{\gamma}{\tilde{\Delta}^5},\\
\gamma &= -a_1a_2(a_1^2 + a_2^2)\cos(\Delta\varpi - 2\sigma) - \frac{a_1^2a_2^2}{8}\\
&\quad [\cos(\Delta\varpi - 3\sigma) - 26\cos(\Delta\varpi - \sigma) + 9\cos(\Delta\varpi + \sigma)],\\
H_{0020} &= \left(\frac{a_1a_2}{\tilde{\Delta}^3} - \frac{1}{\sqrt{a_1a_2}}\right)\cos(\sigma),\\
H_{0011} &= 2\left(\frac{1}{\sqrt{a_1a_2}} - \frac{a_1a_2}{\tilde{\Delta}^3}\right)\cos(\Omega_2 - \Omega_1 - \sigma).
\end{aligned} \tag{9}$$

This expression for $\mathcal{H}_2$ is equivalent to the one reported in Robutel & Pousse (2013), but avoiding the complex notation. We also want to remark that, due to the d'Alembert rules, only even powers of eccentricities and inclinations are present in $\mathcal{H}_2$.

The first-order average Hamiltonian, given by the expression $\mathcal{H}_2$, is not valid in the region of QS because the fast angle $(\lambda_1 + \lambda_2)$ has a similar period to that of the resonant one (σ).[1]

The integrable approximation $\mathcal{H}_{00}$, associated with the circular and planar resonant problem, has been used by some authors to study the motion inside the resonance because it should provide qualitative information about the system dynamics. However, this approximation is inadequate to describe the real dynamics of the planets, even in some simple cases. For evidence, compare the integrations projected in the plane (u, σ) using the analytic expansion $\mathcal{H}$ with the results from the integrable approximation $\mathcal{H}_{00}$. Then,

$$u = \frac{\sqrt{\mu_1\mu_2}}{\sqrt{\mathcal{G}m_0}}\,\frac{\beta_1\beta_2}{(\beta_1 + \beta_2)}\,\frac{(\sqrt{a_1} - \sqrt{a_2})}{(\beta_1\sqrt{\mu_1a_1} + \beta_2\sqrt{\mu_2a_2})} \tag{10}$$

is the dimensionless non-canonical action-like variable.

In Fig. 2, we compare the evolution of the initial conditions in the plane (σ, u) using the integrable approximation $\mathcal{H}_{00}$, the analytical expansion $\mathcal{H}$ and *N*-body simulations. From left to right, the initial conditions correspond to two Jupiter-like planets in coplanar quasi-circular orbits ($e_i = 0.01$) and in eccentric orbits ($e_i = 0.15$), and two Earth-like planets in eccentric orbits ($e_i = 0.15$). The initial conditions are set for $\sigma = 2^\circ$, 60°, 180° and 300° for different u values around zero. Consequently, the semi-major axes are

$$a_i = \overline{a}\left(1 + (-1)^{i+1}\,\frac{\beta_1 + \beta_2}{\beta_j}\sqrt{\frac{\mu_0}{\mu_j}}u\right)^2 \tag{11}$$

where the parameter $\overline{a}$ is the mean value around which the semi-major axes oscillate, $\overline{a} = 1$ (see Robutel & Pousse 2013). Also,

[1] Recently, Robutel, Niederman & Pousse (2015) proposed a valid rigorous average method for this region.

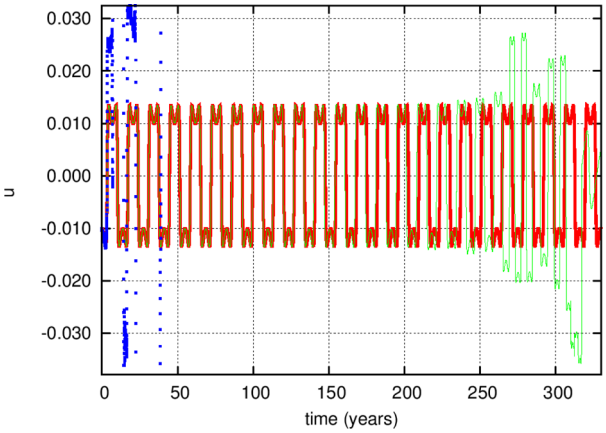

Figure 3. Evolution of u for a coplanar HS pair of Jupiter planets with initial conditions $(u, \sigma) = (-0.01, 180^\circ)$, using $\mathcal{H}_{00}$ (thick red line), $\mathcal{H}$ (green line) and N-body integrations (blue dots). The inclusion of lower-order terms of the eccentricities rapidly excites the system, causing the disruption of the resonance (time $\simeq$250 periods). The N-body simulation rapidly evidences the chaotic nature of this configuration (time $\simeq$5 periods).

the initial conditions for $\Delta\varpi$ are set according to the nearest value of the equilibrium solutions, namely $\sigma \simeq 0^\circ \rightarrow \Delta\varpi = 180^\circ$, and $\sigma \simeq \pm 60^\circ \rightarrow \Delta\varpi = \pm 60^\circ$. The top row shows integrations given by the analytical $\mathcal{H}$ (red dots) and $\mathcal{H}_{00}$ (green lines), while the bottom row shows the same initial conditions, but integrated with a full N-body code. Strictly speaking, our figures depict a projection of the orbital elements on the phase-space portraits. To draw a formal parallel between numerically computed phase-space portraits and their analytic counterparts, a numerical averaging process must be carried out appropriately over the rapidly varying angles. However, for the purposes of this work, we shall loosely refer to these plots as phase-space portraits, since their information content is almost identical.

In the bottom row of Fig. 2, we can see that for Jupiter-like planets, only small-amplitude TP orbits are stable. The remaining conditions are highly unstable (seen as sparsely points) and neither QS nor HS exist for more than a few orbits. Then, we set a threshold to stop the integrations when the mutual distance between the bodies is smaller than the sum of their mutual radius (assuming an Earth or Jupiter radius, depending on the case) or if they exhibit chaotic behaviour that changes their configuration. We also find transitions from HS or TP orbits to QS orbits. Moreover, for quasi-circular orbits ($e_i = 0.01$), it is evident that the integrable approximation (top row) $\mathcal{H}_{00}$ is not good to describe the real dynamics, and that the inclusion of lower-order terms of eccentricities present in $\mathcal{H}$ is enough to destabilize the system. Furthermore, only TP orbits around L_4 and L_5 remain stable (top left-hand and middle panels of Fig. 2). In the right-hand panel of Fig. 2, with moderate initial eccentricities but planetary masses very small, $m_i/m_0 = 3 \times 10^{-6}$, the dynamics predicted by the integrable approximation $\mathcal{H}_{00}$ are similar to $\mathcal{H}$; however, the QS region is only present in the N-body integrations (bottom right-hand panel).

To understand what happens in the HS configuration, Fig. 3 shows an example of the variation of u with time, integrated with different models, for a Jupiter pair of planets. The inclusion of eccentric terms is responsible for instability, even if the initial conditions are quasi-circular orbits ($e_i = 0.01$).

To study the HS configuration, we use the results from Robutel & Pousse (2013), who estimated the size of the HS (U_1) and TP (U_3) regions as:

$$U_1 = \frac{3^{1/6}}{2^{1/3}} \frac{m_1 m_2}{m_0^{1/3}(m_1+m_2)^{5/3}}$$

$$U_3 = \frac{2^{1/2}}{3^{1/2}} \frac{m_1 m_2}{m_0^{1/2}(m_1+m_2)^{3/2}}$$

$$\frac{U_1}{U_3} = \frac{3^{2/3}}{2^{5/6}} \left(\frac{m_0}{m_1+m_2}\right)^{1/6}. \quad (12)$$

Thus, the ratio U_1/U_3 give us the size of the HS region relative to the TP region. As the masses decrease, the relative size increases, but the absolute size is more reduced.

Laughlin & Chambers (2002) mentioned that the HS configuration is not stable for planets more massive than $0.4 M_J$ ($\sim$100 $M_\oplus$) for quasi-circular orbits ($e_i = 0.01$). Recently, Leleu et al. (2015) showed that the HS configuration is stable for systems with masses lower than $\sim$30 $M_\oplus$ ($e_i = 0.05$). Thus, setting the initial conditions very close to the value of U_3 ($1.2U_3$), we numerically integrate the three-body problem for different masses ($m_1 = m_2$) and initial eccentricities ($e_1 = e_2$), and calculate the mean exponential growth factor of nearby orbits (Megno) $\langle Y \rangle$ to analyse their chaoticity (Cincotta & Simó 2000). Fig. 4 shows the values of $\langle Y \rangle$ for 5×10^4 periods for coplanar orbits ($J = 0^\circ$) and initially mutually inclined orbits ($J = 15^\circ$).[2] In the figure, we can identify the allowed maximum mass values as a function of their initial eccentricities for HS planets. These values agree with other authors' results regarding coplanar orbits. We run long-term numerical simulations (10 Myr) for selected initial conditions (especially for $e_i > 0.3$). Those with initial conditions with $\langle Y \rangle \gtrsim 5$ did not survive, maybe due to the long-term diffusion that destabilizes the coorbital systems on a time-scale that varies from 5×10^5 to 8×10^6 periods (see Páez & Efthymiopoulos 2015). Generally, the inclined systems ($J = 15^\circ$) can survive for more periods; however, they are strongly chaotic, and those orbits with $e_i \gtrsim 0.15$ are frequently transition orbits (HS–QS).

We have tested the second-order averaged Hamiltonian $\mathcal{H}_2$, setting the initial conditions near equilibrium configurations with moderate eccentricities ($e_j < 0.3$) and mutual inclinations ($J < 12^\circ$). Moreover, the mean initial Poincaré orbital elements were calculated using a low-pass far-infrared digital filter (Carpino, Milani & Nobili 1987) to eliminate all periodic variations with a period shorter than 3 yr. We selected initial conditions from Table 1 to illustrate the orbital evolution, and the results are shown in Figs 5, 6 and 7. We can see a perfect agreement between the N-body integration and the $\mathcal{H}_2$ model for L_4, AL_4 and the HS configurations, respectively. We resolve the Hamiltonian equations using five and six degrees of freedom, i.e. equations (13) and (14), and the results are the same.

We must remark that the integrations with the $\mathcal{H}_2$ model modify the period of the orbital elements. As a consequence, the secular frequencies sometimes depend on the initial values of e and i. Thus, except for very small e and i, the secular frequencies are poorly approximated, which is a problem for the study of the resonances (inside the coorbital resonance), and especially for the LK resonance. For the initial conditions chosen for Figs 5, 6 and 7, the periods of the eccentricities are 20 per cent longer than those determined with the N-body integrations. When we modify the initial

[2] When both planets have masses, it is convenient to work with mutual inclination J, defined as $\cos J = \cos i_1 \cos i_2 + \sin i_1 \sin i_2 \cos(\Omega_1 - \Omega_2)$ (deduced from spherical trigonometry, see Moulton 1914, p. 408).

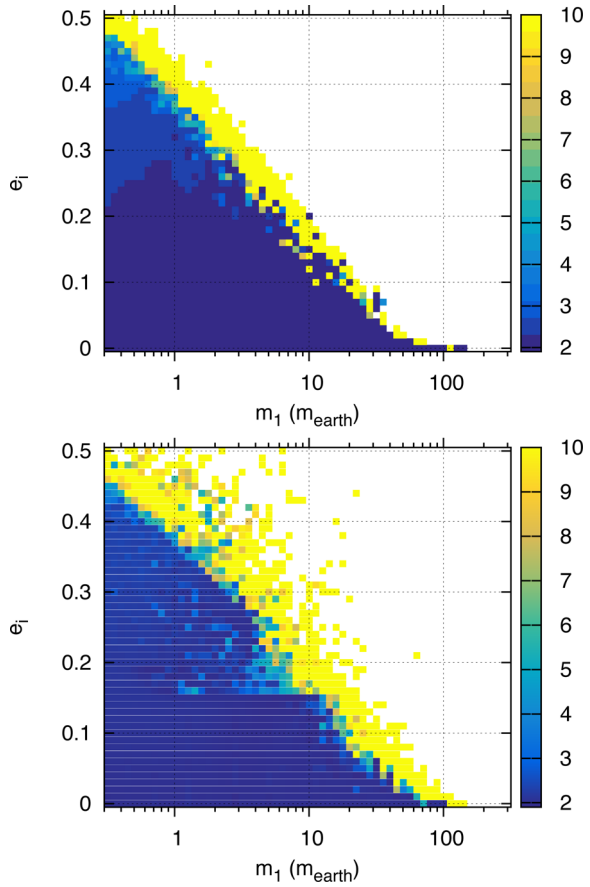

Figure 4. Stability of HS orbits in the plane of osculating initial conditions (m_1, e_i) with $(\sigma, \Delta\varpi) = (60^\circ, 60^\circ)$. Initial values for the semi-major axis are taken from equation (11), setting $u = 1.2U_3$. The colour code indicates the value of $\langle Y \rangle$. Strongly chaotic systems or systems that quit the coorbital resonance before the integration stops are marked with white dots. All coloured orbits survive for at least 10^5 periods. Long-term integrations show that slow chaotic orbits ($\langle Y \rangle \gtrsim 5$) survive from 5×10^5 to 8×10^6 periods, while unstable conditions (in white) do not survive for more than 2×10^3 periods. The initial conditions correspond to coplanar configurations (top panel) and initial mutual inclinations $J = 15^\circ$ (bottom panel).

Table 1. Osculating Poincaré initial conditions near the stable periodic solutions in the $(\sigma, \Delta\varpi)$ plane. All conditions have all angles in degrees, $m_1 = 1M_J$, $m_2 = 0.9M_J$, $a_1 = 1.0038$ au, and $a_2 = 0.995\,784$ au. HS has $u = 0.002$ and masses $m_i = 12.5\ \mathrm{M}_\oplus$.

	σ	$\Delta\varpi$	e_1	e_2	i_1	i_2
L_4	60	60	0.2	0.1	5	3
AL_4	60	240	0.3	0.1	2	12
HS	240	240	0.05	0.05	1	3
QS	0	180	0.45	0.45	1	3

inclinations, the periods can be even four times the real ones. To show this, in the top panel of Fig. 8 we show the secular periods calculated with $\mathcal{H}_2$ and N-body filtered integrations varying the initial eccentricities and two different initial mutual inclinations ($J = 0^\circ$ and $J = 15^\circ$), while in the bottom panel we set the initial eccentricities at $e_1 = e_2 = 0.01$ and $e_1 = e_2 = 0.15$ for different mutual inclinations. The secular frequencies almost do not depend on the initial values of e in the N-body integrations. For near circular orbits and planar orbits, the secular frequencies are approximated well by

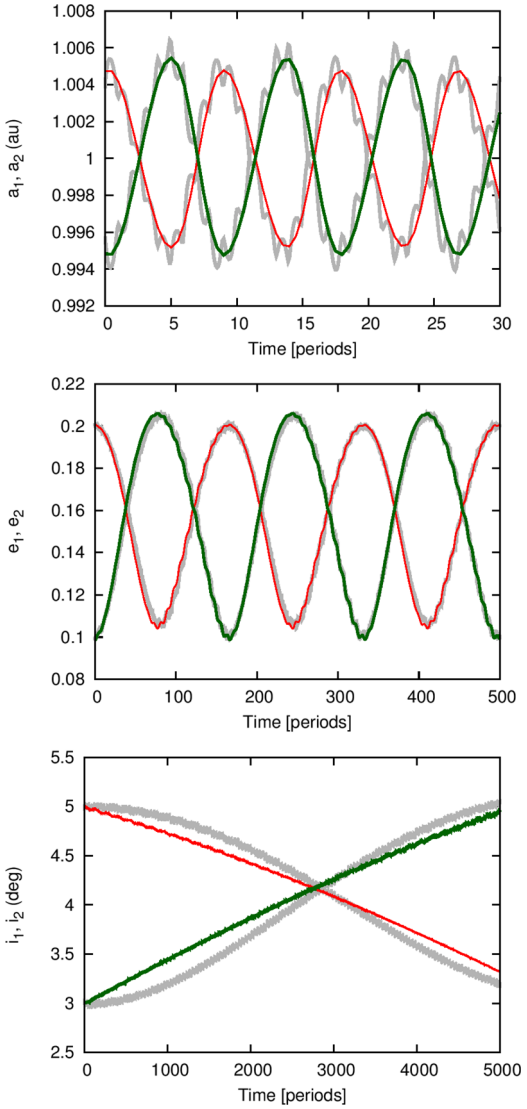

Figure 5. Variation of orbital elements with time using the analytical $\mathcal{H}_2$ model compared with a N-body integration. Amplitudes coincide perfectly and the frequencies were adjusted by hand (see text). Initial conditions from Table 1 for the L_4 case.

$\mathcal{H}_2$. When the eccentricity increases, the frequencies are poorly determined by the $\mathcal{H}_2$ model. In contrast, when we fixed the initial eccentricities at $e = 0.01$ for different mutual inclinations, neither the N-body simulations nor the $\mathcal{H}_2$ model have constant secular frequencies (bottom panel of Fig. 8).

3 SEMI-ANALYTICAL MODEL

To extend the study of the system to the whole parameter space (e.g. planetary masses, eccentricities, inclinations, etc.), it is useful to construct a semi-analytical model for the coorbital motion. We followed the ideas for the 3D models in other resonances (e.g. Beaugé & Michtchenko 2003), extending the study of the coplanar coorbital model developed in Giuppone et al. (2010).

Our model involves two main steps: first, a transformation to adequate resonant variables; second, a numerical averaging of the Hamiltonian with respect to short-period terms. Both procedures are detailed below.

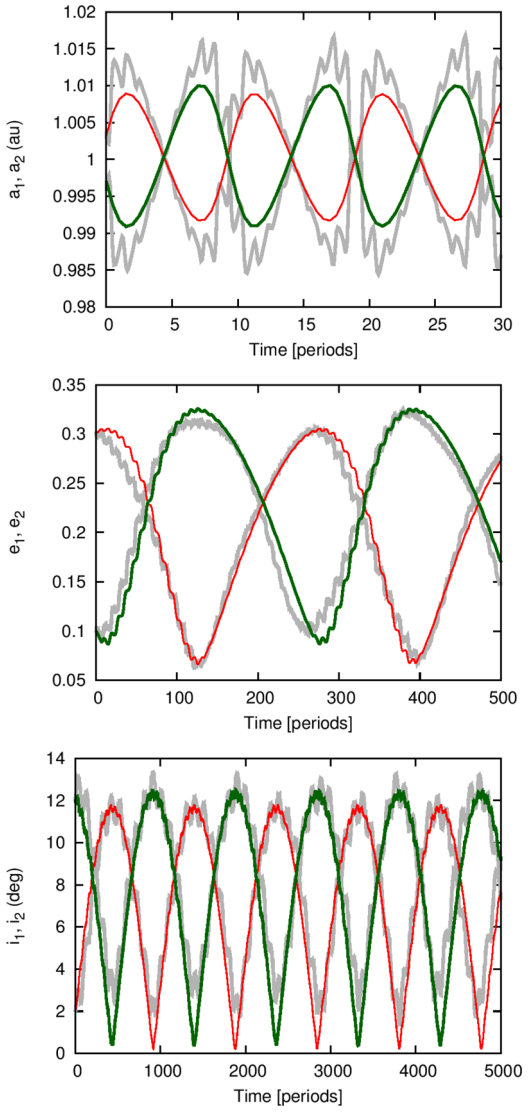

Figure 6. Variation of orbital elements with time using the analytical $\mathcal{H}_2$ model compared with a *N*-body integration. Initial conditions from Table 1 correspond to the AL_4 case.

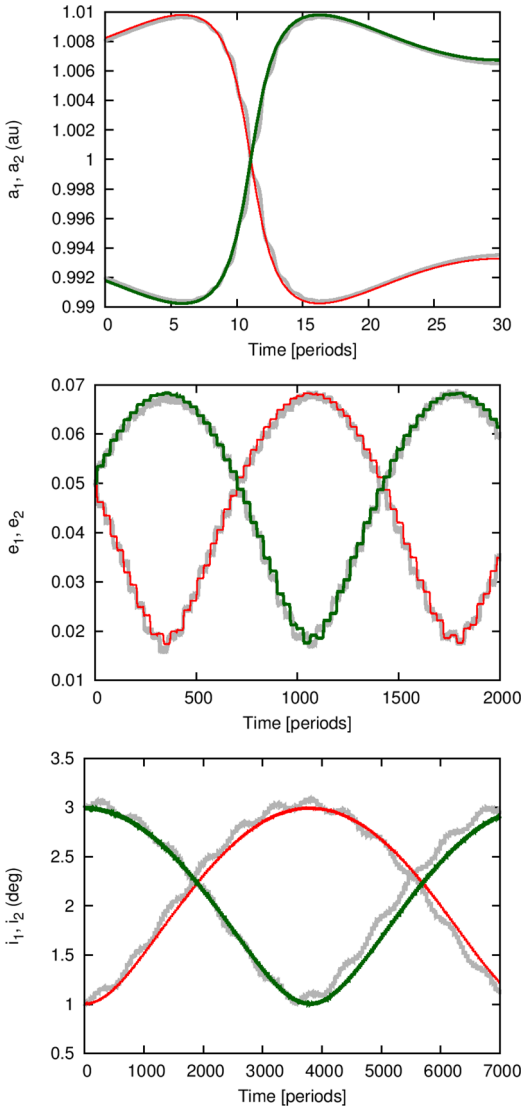

Figure 7. Variation of orbital elements with time using the analytical $\mathcal{H}_2$ model compared with a *N*-body integration. Initial conditions from Table 1 correspond to the HS case.

We begin by introducing the usual mass-weighted Poincaré canonical variables (e.g. Laskar 1990) for each planet with mass m_i:

$$\begin{aligned}
&\lambda_1; && L_1 = \beta_1\sqrt{\mu_1 a_1}\\
&\lambda_2; && L_2 = \beta_2\sqrt{\mu_2 a_2}\\
&p_1 = -\varpi_1; && P_1 = L_1 - G_1 = L_1\left(1-\sqrt{1-e_1^2}\right)\\
&p_2 = -\varpi_2; && P_2 = L_2 - G_2 = L_2\left(1-\sqrt{1-e_2^2}\right)\\
&q_1 = -\Omega_1; && Q_1 = G_1 - H_1\\
&q_2 = -\Omega_2; && Q_2 = G_2 - H_2
\end{aligned} \tag{13}$$

where $\mu_i = \mathcal{G}(m_0 + m_i)$, $G_i = L_i\sqrt{1-e_i^2}$ and $H_i = G_i\cos(i_i)$.

For the initial conditions in the vicinity of coorbital motion, we define the following set of resonant canonical variables (R_1, R_2, S_1, S_2, T_1, T_2, σ, $\Delta\varpi$, s_1, s_2, t_1, t_2), where the new angles and actions are

$$\begin{aligned}
&\sigma = \lambda_2 - \lambda_1; && R_1 = \frac{1}{2}(L_2 - L_1)\\
&\Delta\varpi = p_1 - p_2; && R_2 = \frac{1}{2}(P_1 - P_2)\\
&s_1 = \lambda_1 + \lambda_2 + p_1 + p_2; && S_1 = \frac{1}{2}(L_1 + L_2)\\
&s_2 = -(p_1 + p_2) + (q_1 + q_2); && S_2 = \frac{1}{2}(L_1 + L_2 - P_1 - P_2)\\
&t_1 = q_1 - q_2; && T_1 = \frac{1}{2}(Q_1 - Q_2)\\
&t_2 = -(q_1 + q_2); && T_2 = \frac{1}{2}(H_1 + H_2)
\end{aligned} \tag{14}$$

given that

$$a_1 = \frac{(S_1 - R_1)^2}{\mu_1{\beta_1}^2} \text{ and } a_2 = \frac{(S_1 + R_1)^2}{\mu_2{\beta_2}^2}.$$

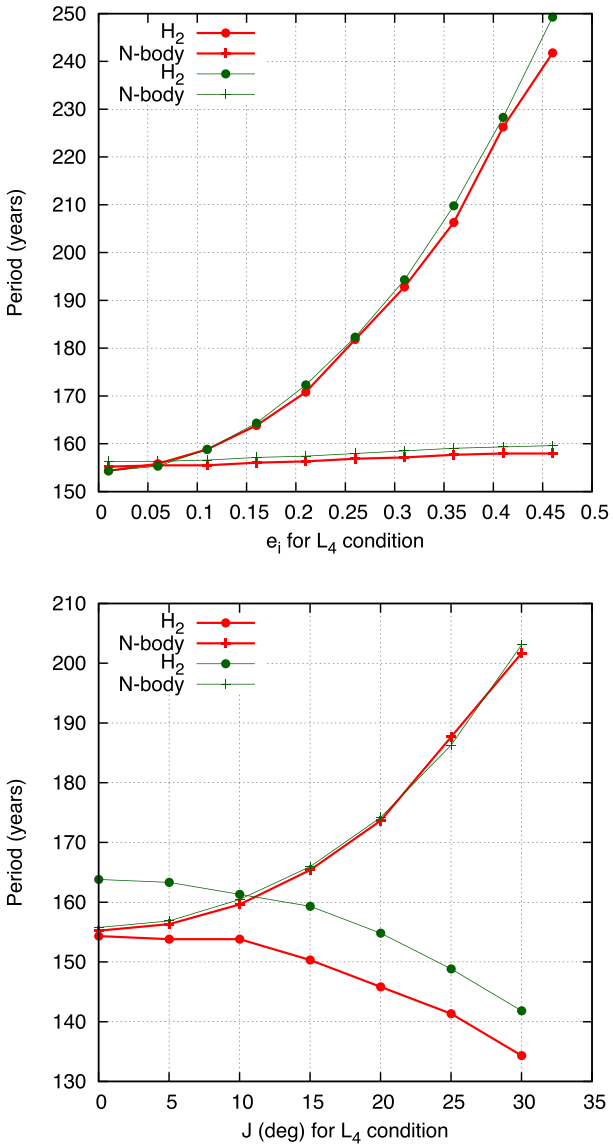

Figure 8. Secular period calculated using the $\mathcal{H}_2$ model (circles) compared with the N-body integration (crosses). Initial osculating angles correspond to the L_4 configuration. Top panel: Thick lines have coplanar initial conditions, while thin lines have initial value $J = 15^\circ$. Bottom panel: Thick lines have quasi-circular initial conditions ($e_i = 0.01$), while thin lines have initial values $e_i = 0.15$.

As we know, a generic argument φ of the disturbing function can be written as

$$\varphi = j_1\lambda_1 + j_2\lambda_2 + j_3\varpi_1 + j_4\varpi_2 + j_5\Omega_1 + j_6\Omega_2, \tag{15}$$

where j_k are integers. In terms of the new angles, the same argument may be written as

$$2\varphi = (j_2 - j_1)\sigma + (j_4 - j_3)\Delta\varpi + (j_1 + j_2)s_1 + \left(\sum_{k=1}^{4} j_k\right) s_2 + (j_6 - j_5)t_1 + \left(\sum_{k=1}^{6} j_k\right) t_2. \tag{16}$$

Since d'Alembert's relation provides a restriction for the j_k coefficients, $\sum_k j_k = 0$, t_2 does not appear in φ (t_2 is a cyclic angle). As a consequence, the associated action T_2 is a constant of motion and we can reduce our problem by one degree of freedom. Hence, our election of canonical variables leads to $T_2 = (1/2)(H_1 + H_2) = (1/2)\mathcal{AM}$ (half the orbital angular momentum of the system).

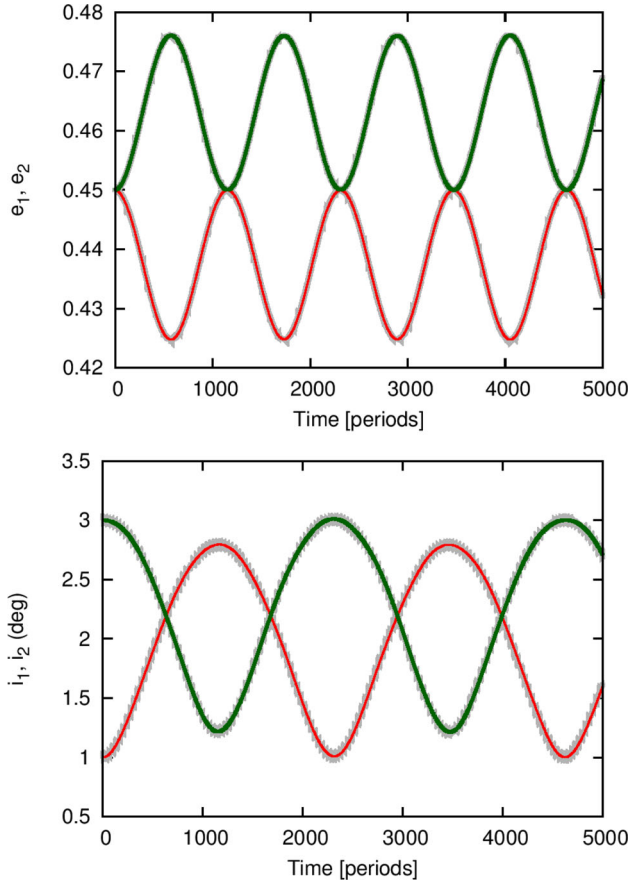

Figure 9. Time variation of eccentricities and inclinations using the semi-analytical model $\bar{\mathcal{H}}$ compared with a filtered N-body integration for the QS condition from Table 1.

Then, the Hamiltonian function can be expressed as $\mathcal{H} = \mathcal{H}_0 + \mathcal{H}_1$, where $\mathcal{H}_0$ corresponds to the two-body contribution:

$$\mathcal{H}_0 = -\frac{\mu_1^2\beta_1^3}{2L_1^2} - \frac{\mu_2^2\beta_2^3}{2L_2^2}. \tag{17}$$

The second term, $\mathcal{H}_1$, is the disturbing function, which can be written as:

$$\mathcal{H}_1 = -\mathcal{G}m_1m_2\frac{1}{\Delta} + \mathcal{T}_1, \tag{18}$$

where Δ is the instantaneous distance between the two planets and $\mathcal{T}_1$ is the indirect part of the potential energy of the gravitational interaction.

Obviously, equations (13) and (14) achieve the same results, but the latter has only five degrees of freedom, imposing the conservation of angular momentum.

The next step is to average the Hamiltonian over the fast angle s_1. This procedure can be performed numerically, allowing us to evaluate the averaged Hamiltonian $\bar{\mathcal{H}}$ as:

$$\bar{\mathcal{H}}(R_1, R_2, S_2, T_1, \sigma, \Delta\varpi, s_2, t_1; S_1, \mathcal{AM}) \equiv \frac{1}{4\pi}\int_0^{4\pi} \mathcal{H}\,\mathrm{d}s_1. \tag{19}$$

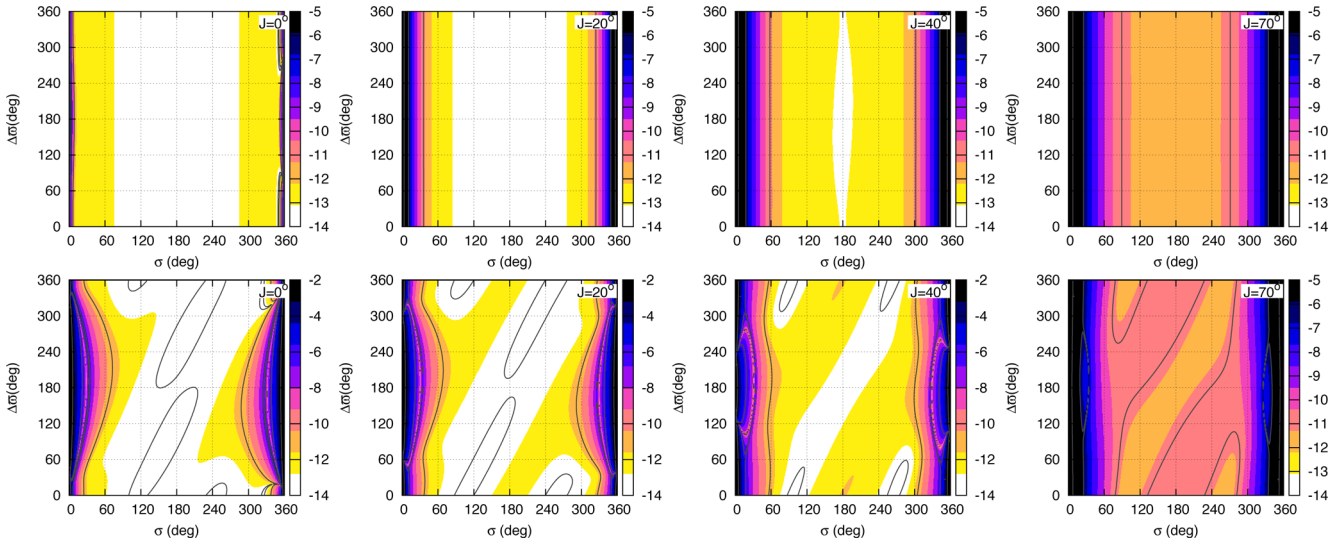

Figure 10. Relative error between the semi-analytical averaged Hamiltonian $\bar{\mathcal{H}}$ and the analytical expansion $\mathcal{H}_2$. We consider two Jupiter-like planets at 1 au with $e_i = 0.01$ (top row) and $e_i = 0.15$ (bottom row). White regions are the most adequate to moderate the dynamics using the $\mathcal{H}_2$ model.

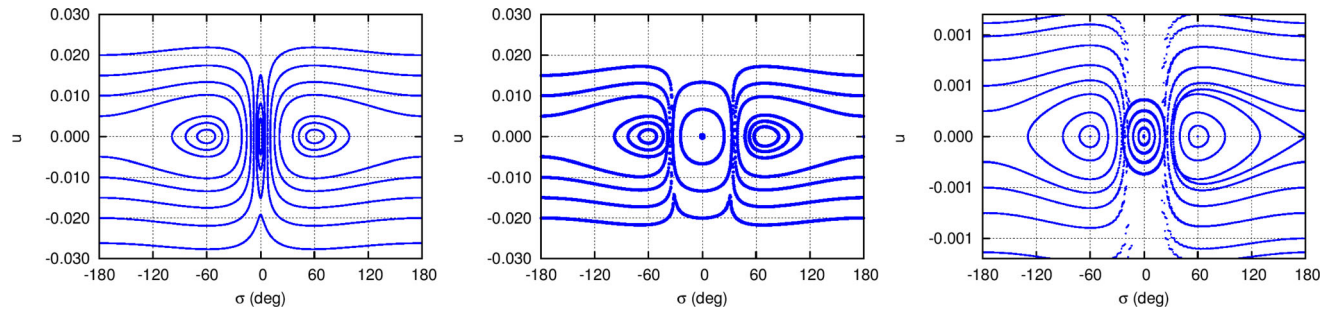

Figure 11. Phase space described by the semi-analytical model $\bar{\mathcal{H}}$ in the plane (u, σ) for the same initial conditions as Fig. 2. Left: Jupiter pair of planets in quasi-circular orbits ($e_i = 0.01$). Middle: Jupiter pair of planets with moderate eccentricities ($e_i = 0.15$). Right: Earth-like planets ($m_i = 3 \times 10^{-6}\,\mathrm{M}_\odot$) in quasi-circular orbits.

In the averaged variables, S_1 is a new integral of motion, which, in analogy to other mean-motion resonances, we identify as the *scaling parameter*, i.e. $\mathcal{K}$.

$\bar{\mathcal{H}}$ constitutes a system with four degrees of freedom in the canonical variables (R_1, R_2, S_2, T_1, σ, $\Delta\varpi$, s_2, t_1), parametrized by the values of both $\mathcal{K}$ and $\mathcal{AM}$. Since the numerical integration depicted in equation (19) is equivalent to a first-order average of the Hamiltonian function (e.g. Ferraz-Mello 2007), only those periodic terms with $j_1 + j_2 = 0$ remain in $\bar{\mathcal{H}}$ (see equation 16).

We have compared the semi-analytical model averaged over the fast angle with the filtered N-body integrations. The filter was made using a low-pass far-infrared digital filter (Carpino et al. 1987) to eliminate all periodic variations with a period shorter than 3 yr. Needless to say, these results match better than those reproduced by the second-order Hamiltonian $\mathcal{H}_2$, but are much slower. Since we do not have restrictions for any configuration, $\bar{\mathcal{H}}$ is more adequate in the whole coorbital resonance. As an example, in Fig. 9 we show the results for an initial condition corresponding to a QS orbit. No significant differences are appreciated for actions, angles, frequencies or orbital elements.

Moreover, combining the information from equation (13) with the expansions in equation (9), we easily identify S_1, S_2 and T_2 as constants of motion. Thus, we can deduce the coupling in the orbital elements in the averaged models, namely

$$\begin{aligned} \beta_1\sqrt{\mu_1 a_1} + \beta_2\sqrt{\mu_2 a_2} &= \text{const}, \\ L_1 {e_1}^2 + L_2 {e_2}^2 &\simeq \text{const}, \\ L_1 {e_1}^2 \cos(i_1) + L_2 {e_2}^2 \cos(i_2) &\simeq \text{const}. \end{aligned} \tag{20}$$

From the previous equations, the coupling between e and i present in the LK resonance is not obvious (see Section 4).

We explore the parameter space $(\sigma, \Delta\varpi)$ and plot the relative difference between the mean Hamiltonian $\bar{\mathcal{H}}$ and the average $\mathcal{H}_2$ model. The QS region[3] shows more discrepancy, even considering Neptune-like planets in quasi-circular orbits. Fig. 10 is a colour map in the plane $(\sigma, \Delta\varpi)$ for two Jupiter-like planets with quasi-circular initial conditions, $e_i = 0.01$, and in eccentric orbits, $e_i = 0.15$. Also, we identify the initial mutual inclination J in each panel. Outside the QS region, the relative difference between Hamiltonians does not exceed 10^{-14}, justifying the region of validity for the $\mathcal{H}_2$ model. Furthermore, analytical models valid for the QS or 'eccentric retrograde satellite orbits', were developed by Mikkola et al. (2006) and

[3] The region defined around $(\sigma, \Delta\varpi) = (0°, 180°)$. See Giuppone et al. (2010) to identify the regions of motion within coorbital resonance.

Sidorenko et al. (2014), but are only valid for the RTBP, considering small inclinations.

To illustrate the validity of this semi-analytical model, Fig. 11 shows the integrations for the same initial conditions as Fig. 2. Obviously, if the mutual inclination J or eccentricities e_i increases, the analytical Hamiltonian $\mathcal{H}_2$ is more inexact. The semi-analytical model eliminates the short periodic terms, making it easier to identify the different types of motion.

4 PHASE SPACE IN THE 3D CASE

Our intention in this section is to find the different types of stable orbits present in the inclined systems for 1:1 MMR.

Voyatzis, Antoniadou & Tsiganis (2014) studied systems that migrate under the influence of dissipative forces that mimic the effects of gas-driven (type II) migration. They demonstrated that sometimes excitation of inclinations occurs during the initial stages of planetary migration. In these cases, *vertical critical orbits* may generate stable families of 3D periodic orbits, which drive the evolution of the migrating planets to non-coplanar motion. Their work focuses on the calculus of the vertical critical orbits of the 2:1 and 3:1 MMRs, for several values of the planetary mass ratio. In hierarchical systems, the secular LK resonance provides conditions for periodic orbits for inclined systems, and its centre of libration is located at $\omega = \pm 90^\circ$ (e.g. Lidov 1961; Kozai 1962; Kinoshita & Nakai 2007). The secular Hamiltonian of RTBP (expanded up to quadrupole order in the semi-major axis ratio a_1/a_2 and averaged with respect to the fast periods λ_1 and λ_2) does not depend on Ω. Hence, its conjugated action is a constant; consequently,

$$\sqrt{\mathcal{G}\, m_0\, a(1-e^2)}\, \cos(i) = \text{const.} \tag{21}$$

Evidence of LK resonance for planetary systems was found in the 2:1 MMR (Antoniadou & Voyatzis 2013) and compared with the circular RTBP. As was pointed out by Libert & Tsiganis (2009), the stability of some inclined exoplanetary systems may be associated with the LK resonance. Moreover, Morais & Namouni (2016) showed that the LK resonance is present for retrograde orbits as well as in prograde orbits and it plays a key role in coorbital resonance capture for circular RTBP.

The LK resonance occurs in hierarchical planetary systems and can be identified dynamically. The centre of this resonance occurs when the mutual inclination between the bodies and the shape of their orbits remain *frozen* in the integration. This occurs at $\Delta\varpi = \pm 90^\circ$. Thus, we identify the centre of LK resonance throughout different dynamical maps when the amplitude of oscillation for e, J and ω tends to zero.

In our development, we average over the sum $\lambda_1 + \lambda_2$ instead of λ_1 and λ_2, obtaining new conserved quantities. Nonetheless, at the limit when the mass ratio goes to zero ($m_2/m_1 \to 0$), we recovered the results from RTBP, from conservation of angular momentum (see equations 14 and 21).

Fig. 12 shows the variation of oscillation for e_2 in the plane $(\sigma, \Delta\varpi)$, setting two equal mass planets at low eccentric orbits ($e_1 = e_2 = 0.15$) for several different values of the initial mutual inclinations. In the left-hand panels, where $a_1 = a_2$, when the initial mutual inclination is low, we can identify QS orbits at (0°, 180°), L_4 at (60°, 60°) and AL_4 at ($\simeq$70°, $\simeq$250°). As the initial mutual inclination increases, the regions of periodic orbits shrink. Only the L_4 condition is robust and it survives even for $J = 36^\circ$ (tiny dark region in the bottom panel). We have realized that setting $a_1 = a_2$ does not give any further information about the possible existence of HS or the LK resonance. Thus, following our results from Section 2,

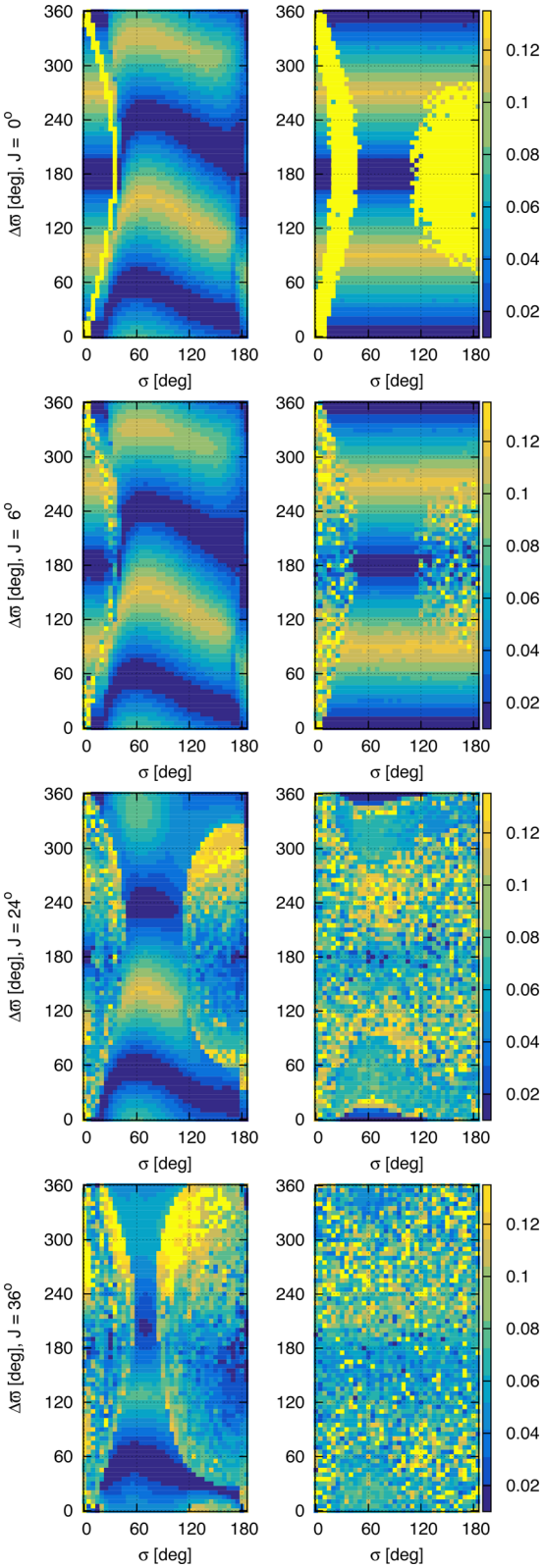

Figure 12. Initial conditions integrated for 10^4 periods with $e_1 = e_2$ and $m_1 = m_2 = 4\ \mathrm{M}_\oplus$. Initial conditions for the left column have $a_1 = a_2 = 1$ au, while for the right column $a_1 = 1.004\,838$ and $a_2 = 0.995\,17$ au. The colour scale represents the amplitude variation of e_2. Each row corresponds to a different initial J.

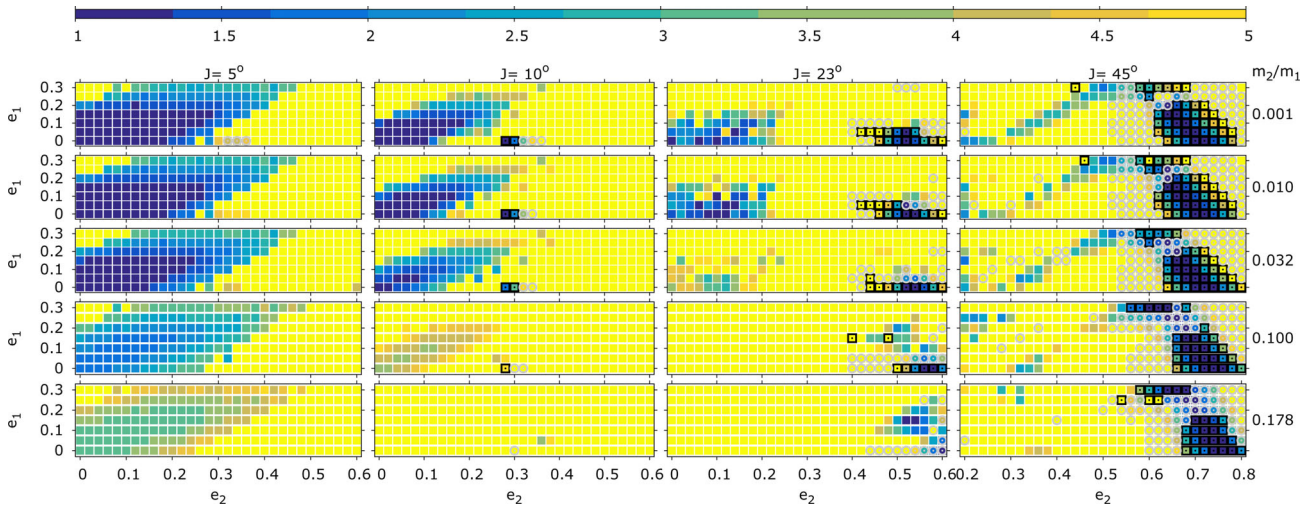

Figure 13. Initial conditions integrated for 10^5 periods. Black squares correspond to amplitudes of $\omega_2 < 10^\circ$ and grey circles to $10^\circ < \omega_2 < 20^\circ$. For the remaining initial conditions, ω_2 circulates very slowly. The colour scale is proportional to the oscillation variation of J.

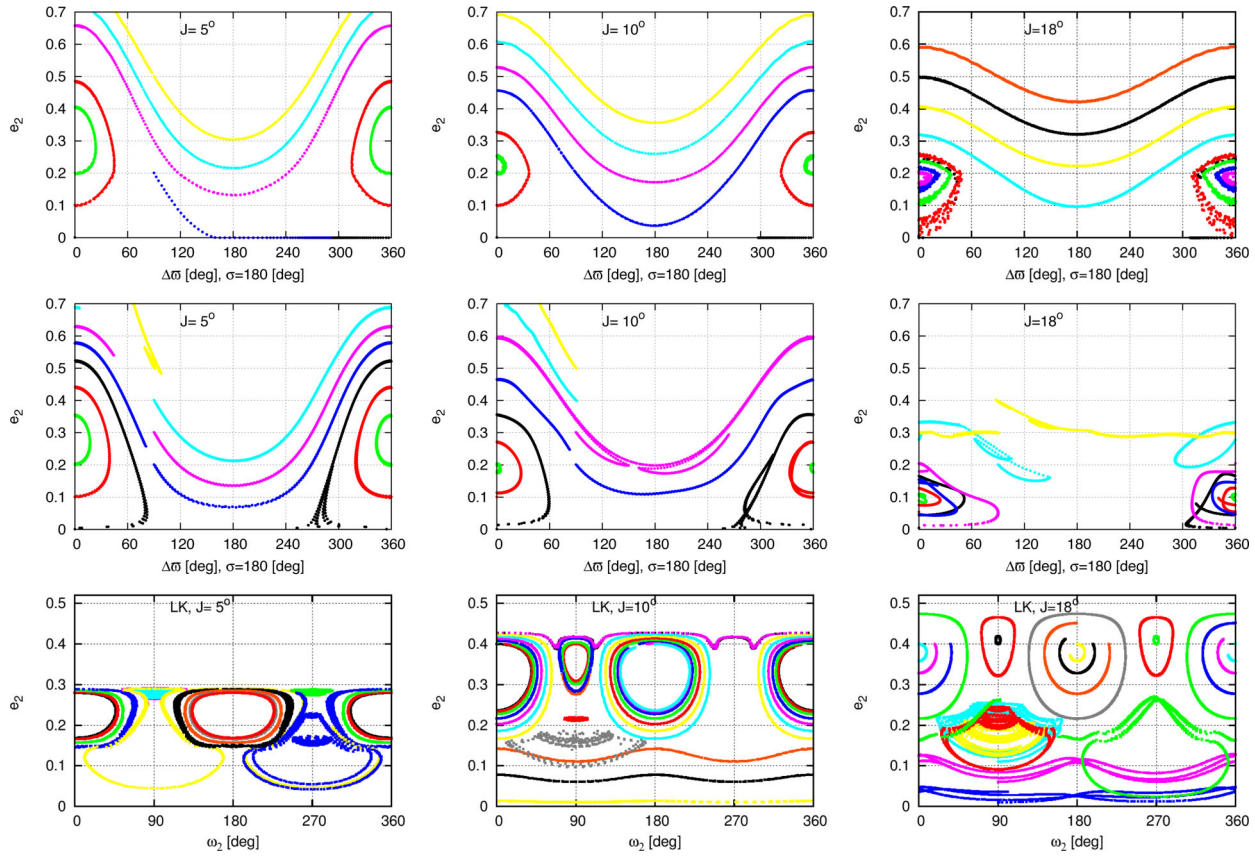

Figure 14. Phase space for a given value of $\mathcal{AM}$ and different initial mutual inclinations ($J = 5^\circ$, $J = 10^\circ$ and $J = 18^\circ$ from left to right). The first and second rows correspond to the phase space using $\mathcal{H}_2$ and N-body integrations for 3×10^5 periods, respectively, in the plane $(\Delta\varpi, e_2)$, while the bottom row corresponds to integrations on the plane (ω_2, e_2) with $m_1 = 3 \times 10^{-6}\,\mathrm{M}_\odot$ and $m_2 = 3 \times 10^{-9}\,\mathrm{M}_\odot$. Each colour represents the evolution of a different initial condition.

we set $u = 1.2U_3$ ($a_1 = 1.004\,838$ and $a_2 = 0.995\,17$), showing the results in the right column of Fig. 12. There, the HS region appears at $\Delta\varpi = 0^\circ$, 180°; however, it is not present for $J = 0^\circ$ at $(\sigma, \Delta\varpi) = (\simeq 180^\circ, \simeq 180^\circ)$.[4]

[4] Besides, it is present for $J = 0^\circ$ with $a_1 = a_2$. Its Megno value shows that it is highly chaotic.

To optimize the identification of the region where the LK configuration appears, we study the plane (e_1, e_2) and initial conditions with $\omega_2 = 90^\circ$, $\sigma = 180^\circ$, $t_1 = 180^\circ$, $\Delta\varpi = s_1 = s_2 = 0^\circ$ and $u = 1.2U_3$. In this plane, we varied J for different mass ratios, ranging from $\log(m_2/m_1) = -3$ to 0. Fig. 13 summarizes the results with a colour scale proportional to the variation of the mutual inclination J. We identify two regions of periodic orbits. One region

corresponds to $e_1 \simeq e_2$, which is easier to identify for low mutual inclination (see the first column, $J = 5^\circ$), and the other corresponds to $e_1 \simeq 0$ and $e_2 > 0.3$ depending on J and the mass ratio, which we refer to as the LK region. For a very low mass ratio, $m_2/m_1 \simeq 0.001$ (near RTBP conditions, top row in the figure), it is easy to find the LK resonance in the range of mutual inclination $10^\circ < J < 50^\circ$. This configuration is only found up to $m_2/m_1 \simeq 0.178$ for very high values of e_2.

In Fig. 14, we plot both regions in the parameter space, setting $m_2/m_1 \simeq 0.001$. The top and middle rows show integrations with the $\mathcal{H}_2$ model and the N-body code, respectively, in the HS region on the plane $(\Delta\varpi, e_2)$. We used the same colours in all panels to facilitate a comparison between them. Evidently, the $\mathcal{H}_2$ model is limited to small (or even moderate) inclinations and eccentricities, reproducing very well the parameter space with the oscillation centres slightly displaced. We numerically verified that the results are indistinguishable when using $m_2 = 0$ (RTBP) or $m_2/m_1 = 10^{-3}$. Although, the systems are well reproduced for moderate mutual inclinations, the interactions between the bodies are evident for some orbits, showing chaotic motion in the N-body integrations.

On the other hand, in the bottom row of Fig. 14 we show the LK region on the plane (ω_2, e_2) for the same values of initial J. The results for LK at $J = 18^\circ$ agree with Namouni (1999) for the RTBP inside the 1:1 MMR. The LK region is a mixture of dynamical regimes and it was insightfully depicted numerically by Namouni (1999). In Fig. 15, we show these different kinds of motion in the plane (u, σ) for $J = 18^\circ$ using the same colours and conditions as in the bottom right-hand panel of Fig. 14. In the region of low eccentricities, the motion is of HS type and ω_2 circulates. Regions at $\omega_2 = 0^\circ$ or 180°, where ω_2 librates with moderate values of e_2, are those corresponding to passing orbits. We can identify the LK resonance at $\omega_2 = \pm 90^\circ$ with $e_2 \simeq 0.4$ (where ω_2 librates). Near to the LK resonances, there is a vase-like domain where transitions between HS and QS orbits are present. However, the analytical $\mathcal{H}_2$ model was not able to reproduce the structure of the phase space. Also, the phase space for $J = 5^\circ$ shows only transition orbits and temporary HS–QS orbits.

To summarize the location of the LK resonance, we plot in the plane (e_2, J) the amplitude of oscillation of J, setting $e_1 = 0$ for different mass ratios (see Fig. 16). We can perfectly identify that the LK resonance is present up to $J \simeq 50^\circ$ and its appearance strongly depends on the mass ratio. Thus, for example, Earth-like planets can be in the centre of the LK resonance at low or high inclinations. In Fig. 17, we plot only the points corresponding to the minimum

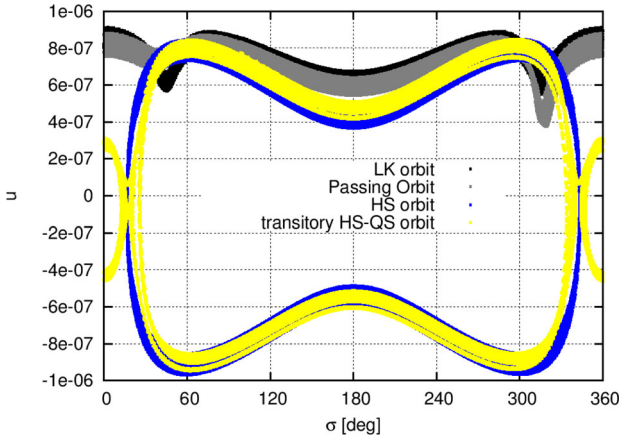

Figure 15. Examples of dynamical regimes present in Fig. 14. See text for more details.

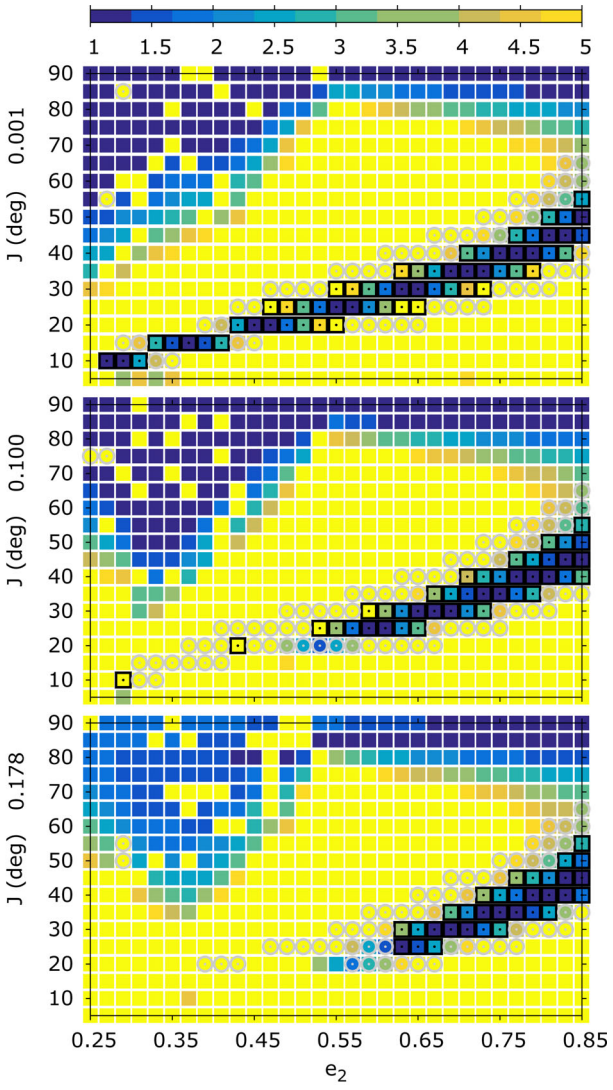

Figure 16. Location of LK resonance centre depending on mass ratio and initial mutual inclination. The more massive planet has a circular orbit $e_1 = 0$ with remaining orbital elements as in Fig. 13. The initial conditions were integrated for 10^5 periods. Black squares correspond to an amplitude of $\omega_2 < 10^\circ$ and grey circles to $10^\circ < \omega_2 < 20^\circ$. For the remaining initial conditions, ω_2 circulates very slowly.

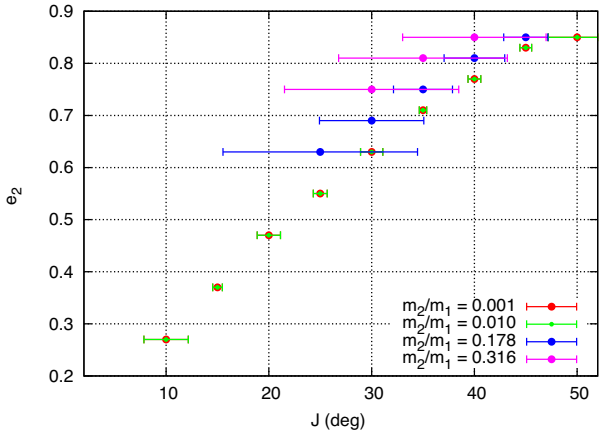

Figure 17. Location of the LK resonance centre depending on the mass ratio and the initial mutual inclination. Error bars are proportional to the oscillation of ω_2.

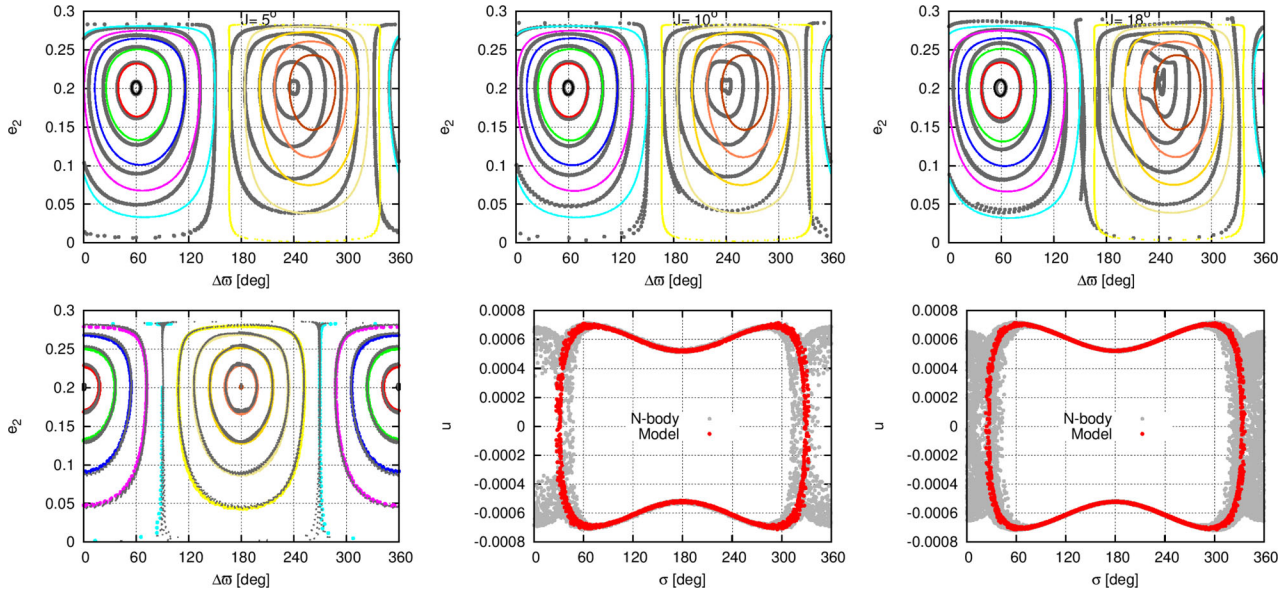

Figure 18. Phase space for a given value of $\mathcal{AM}$ and initial mutual inclination $J = 5^\circ$, $J = 10^\circ$ and $J = 18^\circ$ (from left to right). Top row: Two Jupiter-like planets with $a_1 = a_2 = 1$ and $\sigma = 60^\circ$ (Lagrangian region). Bottom row: Two planets in the HS region, with mass $3 \times 10^{-6}\,M_\odot$, $\sigma = 180^\circ$ and $u = 1.2U_3$. We plot with grey dots the N-body integrations and with colours the $\mathcal{H}_2$ model integrations.

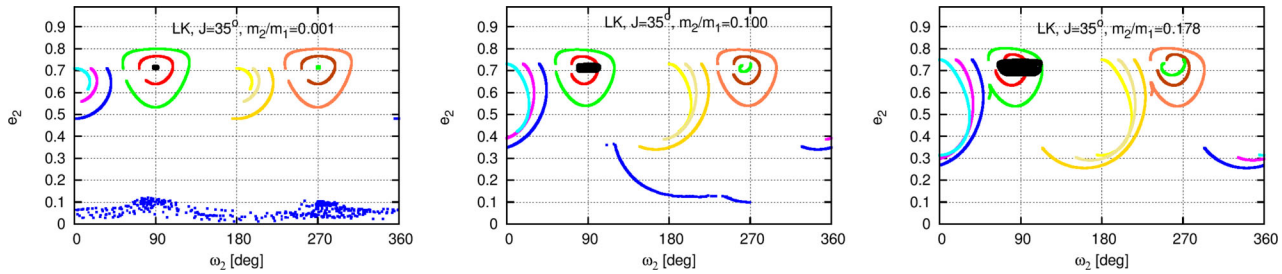

Figure 19. Phase space for a given value of $\mathcal{AM}$ to show the LK resonance centre for $J = 35^\circ$ for three different mass ratios.

amplitude of oscillation of J for several mass ratios. When $m_2/m_1 \to 0.3$, the LK resonance almost dissipates and the strong interactions cause the amplitude of oscillation for ω_2 to increase. However, they are regular orbits, according to their Megno value $\langle Y \rangle$ ($\lesssim 2.02$).

Unlike in Fig. 14, the general problem (both planets with similar masses) is slightly different, and easier to analyse on the plane $(\Delta\varpi, e_2)$. The averaged analytical $\mathcal{H}_2$ model works well even for high inclinations and we are able to analyse the structure depicted by numerical integrations. Fig. 18 shows the phase space for three different mutual inclinations J and moderate eccentricities (initially, $a_1 = a_2 = 1$ au, $m_1 = m_2 = 3 \times 10^{-6}\,M_\odot$ and $e_1 = e_2 = 0.2$). When the initial conditions have $\sigma = 60^\circ$ (top row), we can easily identify two islands of stability corresponding to the L_4 configuration (at $\Delta\varpi = 60^\circ$) and the AL_4 configuration (at $\Delta\varpi \simeq 240^\circ$). The L_4 region is very well depicted by the model, even for $J = 18^\circ$, but the AL_4 region artificially shifts the centre for $\Delta\varpi \to 270^\circ$; besides the amplitude of e_2 is well represented. This effect is due to the limitations of expansions. For quasi-circular orbits, this shift vanished.

In the bottom row of Fig. 18, when $\sigma = 180^\circ$, we set $u = 1.2U_3$. The oscillation centres are around $\Delta\varpi \simeq 0^\circ$ and $\Delta\varpi \simeq 180^\circ$. Indeed, the central point with $\Delta\varpi \simeq 180^\circ$ may correspond to the Euler configuration L_3 ($J \to 0^\circ$), which is unstable in the RTBP. When J increases, this family is the only one that survives, although it seems chaotic in this plane. The other centre, around $\Delta\varpi \simeq 0^\circ$, corresponds to the family identified as unstable by Hadjidemetriou et al. (2009) and Hadjidemetriou & Voyatzis (2011) in the coplanar planetary problem, using Jupiter planets. For $J \lesssim 20^\circ$, the model perfectly matches the N-body integration. After that, this region becomes unstable. We plot results in the projected plane (σ, u) for $J = 10^\circ$ and $J = 18^\circ$ to show that chaotic orbits in this region correspond to HS–QS transition orbits (N-body integration with grey points). However, the general behaviour of HS is captured by the $\mathcal{H}_2$ model.

We tested a wide variety of systems with equal mass planets, from two Earth-mass planets to two Jupiter-mass planets with mutual inclinations as high as 60° in the region previously identified as LK. We did not find evidence of LK resonance. For high mutual inclinations, the systems are indeed strongly chaotic, and regular motion is allowed very close to the exact location of L_4 or AL_4, and the region around L_4 is broader.

Also, it is important to remark that as the mutual inclination is greater than 10°, the systems exhibit chaotic behaviour if the initial conditions do not correspond to the equilibrium solution ($e_1 = e_2$ for $m_1 = m_2 = 1\,M_\oplus$). Nevertheless, we find some systems initially located at high mutual inclinations that could be in coplanar orbits after scattering.

The N-body integrations of Fig. 19 show examples of LK phase portraits in the plane (ω_2, e_2) for $J = 35^\circ$ and different mass ratios, with $m_1 = 1\,M_\oplus$ and $e_1 = 0.001$. Note the centre of LK resonance

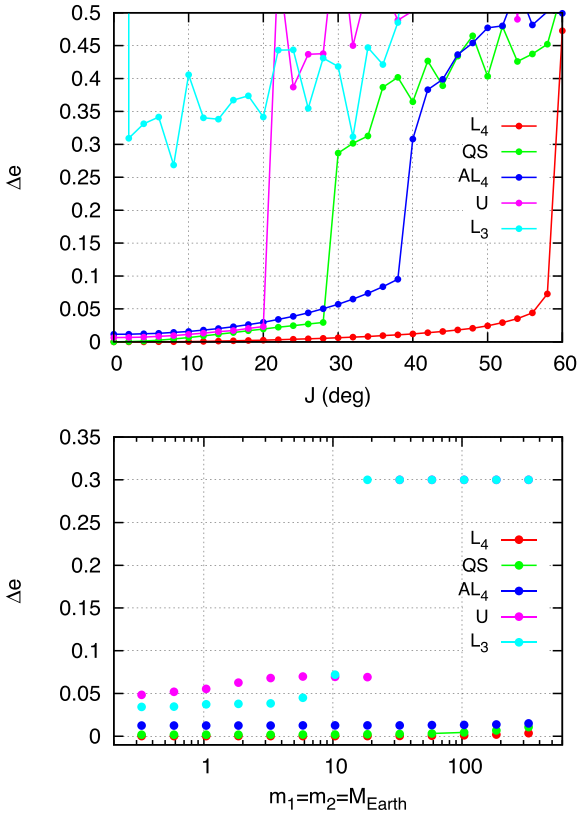

Figure 20. Analysis of periodic orbits L_4, AL_4, QS, L_3 and U in the non-coplanar case using as an indicator the variation of Δe_2. Results correspond to N-body integrations for 10^6 periods. Top: Results considering two planets with masses $m_1 = m_2 = 4\ M_\oplus$ and $e_i = 0.15$. The smooth variation of Δe_2 when we increase J is a good indicator of regular orbits ($\langle Y \rangle \simeq 2$), although almost all the orbits survive at least for 10^6 periods. Bottom: Analysis of stability for inclined systems depending on their masses (see text for more details).

located at $\omega_2 = \pm 90^\circ$. The low eccentric regime, $e_2 \lesssim 0.2$, is usually chaotic for this value of J. We use different colours to identify the evolution of initial conditions integrated for 3×10^5 periods, while the condition corresponding to $\omega_2 = 90^\circ$ was integrated over 10^7 periods. Is easy to see the importance of the forced oscillation around the LK centre when $m_2/m_1 \to 0.2$, justifying the error bars in Fig. 17.

Finally, we analyse the 3D configurations for periodic orbits mentioned in Fig. 1: L_4, AL_4, QS, L_3 and U. To construct the families of periodic orbits in the spatial case, we began from the previously known results in the planar case and varied the mutual inclinations J. For each family, we checked that $\dot{\sigma} = \Delta\dot{\varpi} = 0$, setting the remaining angles equal to zero. We believe that this is a natural extension from the periodic orbits in the equal-mass planar case, although a more rigorous search should use the local extrema of the semi-analytical Hamiltonian. The top panel in Fig. 20 shows the variation of the amplitude of oscillations for e_2, Δe_2, for systems with different initial mutual inclinations and integrated over 10^6 periods. For the L_4, AL_4 and QS orbits, we set the initial semi-major axes $a_i = 1$ au, while for L_3 and U, we set a_i using $u = 1.2U_3$. We calculate the Megno value for every orbit $\langle Y \rangle$, but we choose to show the Δe_2 indicator because it is easier to see the smooth *degradation* of orbits as J increases; alternatively, ΔJ is a good indicator too. The most regular orbits are those corresponding to L_4 configurations (even for $J \simeq 60^\circ$). AL_4 orbits are regular when $J \lesssim 38^\circ$ and QS orbits are regular up to $J \lesssim 28^\circ$. On the other hand, U-type configurations remain stable and bounded for the chosen planetary masses (4 $M_\oplus$) when $J \lesssim 20^\circ$, although the evolution of orbital elements shows a slow diffusion of chaos. The L_3 orbits are also interesting. For $J = 0$, the orbits are unstable, yielding close encounters between the planets; however, for $J > 0$, the orbits become stable for at least 10^6 periods ($\langle Y \rangle > 5$). Even for $J \simeq 60^\circ$, the orbits oscillate around $\Delta\varpi = 180^\circ$, although when $0^\circ < J < 20^\circ$, their chaoticity is more bounded.

The bottom panel of Fig. 20 shows Δe_2, attained during the integrations, for several mass values for a pair of planets. We choose to show $J = 5^\circ$ to illustrate the general behaviour of the families. The L_4, AL_4 and QS configurations are regular and robust configurations in the range $0.3\,M_\oplus < m_i < 1 M_J$. The U-type orbits seem to be regular for masses $m_i \lesssim 10\ M_\oplus$, despite that long-term diffusion is observed, and they remain in this configuration at least for 1 Gy. In contrast, for systems with more massive planets ($m_i \gtrsim 20\ M_\oplus$), close encounters cause the expulsion of one planet ($a_i > 2$ au) in less than 10^4 periods. This same limit was observed for the coplanar case. The L_3 configurations are chaotic but bounded for $m_i \lesssim 15\ M_\oplus$ and, also like U configurations, after this value of masses the systems are quickly destroyed.

5 CONCLUSIONS

We studied the three-body problem in the context of coorbital resonance, considering coplanar and spatial configurations. We followed several approaches: analytical ($\mathcal{H}$), averaged analytical ($\mathcal{H}_2$, equations 9) and semi-analytical ($\bar{\mathcal{H}}$, equation 19). We found appropriate angles and actions (equations 14) that evidence the conserved quantities, verifying the results with N-body integrations. Some tests were carried out in the limit of the RTBP.

We analysed the orbital evolution using the different models, and identified the regular and chaotic regions in the plane (σ,u) for massive planets. In fact, the phase-space structure given by the integrable approximation $\mathcal{H}_{00}$ is not adequate for any condition, and our semi-analytical model is more accurate (see Fig. 2). We roughly established a mass limit for the existence of HS orbits when working with two massive planets depending on the eccentricities and mutual inclinations (see Fig. 4).

The analytical $\mathcal{H}_2$ model described correctly the resonant motion up to moderate eccentricities ($e_i \leq 0.3$) and initial mutual inclinations ($J \leq 35^\circ$), which always occurs outside the region associated with QS motion. Using the $\mathcal{H}_2$ model, we speeded the orbital evolution by a factor of ~50. However, depending on the particular problem, the secular frequencies are overestimated (even 10 times in our examples). The three effects mentioned (Tides, YARKOVSKY and YORP) are dissipative. Yarkovsky effect is induced by the thermal emission forces on the asteroid's surface (e.g. Bottke et al. 2002). YORP effect alters the rotation rate of asteroids and the orientations of their rotation axes (e.g. Golubov et al. 2016 and references there in).

The analytical $\mathcal{H}_2$ model was accurate for the general three-body problem with high mutual inclinations, while in the context of RTBP, the semi-analytical model $\bar{\mathcal{H}}$ or N-body integrations should be used.

We established the location of LK resonance within the 1:1 MMR. The location of the LK resonance centre strongly depends on the mass ratio and on the mutual inclination. The limit for the existence starts from the case of RTBP until $m_2/m_1 \lesssim 0.3$, though planets with comparable masses force the excitation of the orbits around the equilibrium solution.

Thus, when we considered an inclined pair of planetary systems, the L_4, AL_4 and QS orbits are the most regular, and we discover some interesting and very unexpected results for the U and L_3 orbits. The unstable U orbits identified by Hadjidemetriou et al. (2009) are, in fact, regular and very stable orbits for a pair of Earth-like planets up to mutual inclinations lower than 20°. For inclined systems, unlike the planar problem, the L_3 orbits are very chaotic but bounded. We checked for $J \lesssim 30°$ that the orbits remain stable at least for 50 Myr.

The models developed here can be used for a systematic study of the secular dynamics in the coorbital regime with the Solar system planets, and also, with exoplanetary systems. Further work is necessary to study the families of periodic orbits (and stationary solutions). Moreover, further work is necessary to characterize the change in the phase-space structure of 1:1 MMR and to give rigorous definitions for the families of periodic orbits in the spatial case and their relationship with the planar and also with the restricted cases.

ACKNOWLEDGEMENTS

The authors wish to thank Dr Beaugé for his stimulating suggestions and Dr A. L. Serra for her valuable comments. We acknowledge financial support from CONICET/FAPERJ (2318/15/39593-E26/110.063/2014). The numerical simulations were performed on the local computing resources at Córdoba University (Argentina).

REFERENCES

Antoniadou K. I., Voyatzis G., 2013, Celest. Mech. Dynamical Astron., 115, 161
Beaugé C., Michtchenko T. A., 2003, MNRAS, 341, 760
Bottke W. F. Jr., Vokrouhlický D., Rubincam D. P., Broz M., 2002, in Bottke W. F. Jr., Cellino A., Paolicchi P., Binzel R. P., eds, The Effect of Yarkovsky Thermal Forces on the Dynamical Evolution of Asteroids and Meteoroids. Arizona Press, Tucson, p. 395
Brouwer D., Clemence G. M., 1961, Methods of Celestial Mechanics. Academic Press, New York
Carpino M., Milani A., Nobili A. M., 1987, A&A, 181, 182
Cincotta P. M., Simó C., 2000, A&AS, 147, 205
Dobrovolskis A. R., 2013, Icarus, 226, 1635
Ferraz-Mello S., ed., 2007, Canonical Perturbation Theories – Degenerate Systems and Resonance, Astrophysics and Space Science Library Vol. 345. Springer, US
Ford E. B., Gaudi B. S., 2006, ApJ, 652, L137
Ford E. B., Holman M. J., 2007, ApJ, 664, L51
Golubov O., Kravets Y., Krugly Y. N., Scheeres D. J., 2016, MNRAS, 458, 3977
Giuppone C. A., Beaugé C., Michtchenko T. A., Ferraz-Mello S., 2010, MNRAS, 407, 390
Giuppone C. A., Morais M. H. M., Boué G., Correia A. C. M., 2012, A&A, 541, A151
Hadjidemetriou J. D., Voyatzis G., 2011, Celest. Mech. Dynamical Astron., 111, 179
Hadjidemetriou J. D., Psychoyos D., Voyatzis G., 2009, Celest. Mech. Dynamical Astron., 104, 23
Haghighipour N., Capen S., Hinse T. C., 2013, Celest. Mech. Dynamical Astron., 117, 75
Kinoshita H., Nakai H., 2007, Celest. Mech. Dynamical Astron., 98, 67
Kozai Y., 1962, AJ, 67, 591
Laskar J., 1990, Icarus, 88, 266
Laskar J., Robutel P., 1995, Celest. Mech. Dynamical Astron., 62, 193
Laughlin G., Chambers J. E., 2002, AJ, 124, 592
Leleu A., Robutel P., Correia A. C. M., 2015, A&A, 581, A128
Libert A.-S., Tsiganis K., 2009, A&A, 493, 677
Lidov M. L., 1961, Iskus. sputniky Zemly (in Russian), 8, 5
Mikkola S., Innanen K., Wiegert P., Connors M., Brasser R., 2006, MNRAS, 369, 15
Morais M. H. M., Namouni F., 2016, Celest. Mech. Dyn. Astron., 125, 91
Moulton F. R., 1914, An Introduction to Celestial Mechanics. The Macmillan company, New York
Namouni F., 1999, Icarus, 137, 293
Páez R. I., Efthymiopoulos C., 2015, Celest. Mech. Dynamical Astron., 121, 139
Robutel P., Pousse A., 2013, Celest. Mech. Dynamical Astron., 117, 17
Robutel P., Niederman L., Pousse A., 2015, preprint (arXiv:1506.02870)
Sidorenko V. V., Neishtadt A. I., Artemyev A. V., Zelenyi L. M., 2014, Celest. Mech. Dynamical Astron., 120, 131
Vokrouhlický D., Nesvorný D., 2014, ApJ, 791, 6
Voyatzis G., Antoniadou K. I., Tsiganis K., 2014, Celest. Mech. Dynamical Astron., 119, 221

This paper has been typeset from a TEX/LATEX file prepared by the author.